


## ARTICLE

# Thixomolded AZ91D and MRI153M magnesium alloys and their enhanced corrosion resistance

Ricardo H. Buzolin<sup>1,2,3</sup>  | Polina Volovitch<sup>4</sup> | Alina Maltseva<sup>4</sup> |  
Sviatlana Lamaka<sup>1</sup> | Carsten Blawert<sup>1</sup> | Chamini L. Mendis<sup>5</sup> |  
Andreas Lohmüller<sup>6</sup> | Karl U. Kainer<sup>1</sup> | Norbert Hort<sup>1</sup>

<sup>1</sup>Magnesium Innovation Centre, Helmholtz-Zentrum Geesthacht, Geesthacht, Germany

<sup>2</sup>Christian Doppler Laboratory for Design of High-Performance Alloys by Thermomechanical Processing, Graz, Austria

<sup>3</sup>Institute of Materials Science, Joining and Forming, Graz University of Technology, Graz, Austria

<sup>4</sup>Institute de Recherche de Chimie Paris, Paris, France

<sup>5</sup>Brunel Centre for Advanced Solidification Technology, Brunel University London, Uxbridge, UK

<sup>6</sup>Neue Materialien Fürth GmbH, Fürth, Germany

## Correspondence

Ricardo H. Buzolin, Magnesium Innovation Centre, Helmholtz-Zentrum Geesthacht, Max-Planck-Straße 1 21502, Geesthacht, Germany.  
Email: ricardo.buzolin@tugraz.at

## Abstract

AZ91D and MRI153M alloys were produced by thixomolding. Their corrosion resistance is significantly higher than that of similar materials produced by ingot or die-casting. A corrosion rate smaller than 0.2 mm/year in 5 wt% NaCl solution is measured for the thixomolded AZ91D alloy. The corrosion behaviour was evaluated using immersion tests, electrochemical impedance spectroscopy, hydrogen evolution, glow discharge optical emission spectroscopy, and atomic emission spectroelectrochemistry. A bimodal microstructure is observed for both alloys, with the presence of coarse primary  $\alpha$ -Mg grains, fine secondary  $\alpha$ -Mg grains,  $\beta$ -phase, and other phases with a minor volume fraction. The amount of coarse primary  $\alpha$ -Mg is significantly higher for the AZ91D compared with the MRI153M. The network of  $\beta$ -phase around the fine secondary  $\alpha$ -Mg grains is better established in the thixomolded AZ91D alloy. A combination of several factors such as the ratio of primary to secondary  $\alpha$ -Mg grains, localised corrosion or barrier effect due to other phases, as well as regions of preferential dissolution of the  $\alpha$ -Mg due to chemical segregation, are thought to be responsible for the high corrosion resistance exhibited by the thixomolded AZ91D and MRI153M.

## KEYWORDS

AZ91D, corrosion resistance, hydrogen evolution, magnesium alloys, MRI153M, thixomolding

## 1 | INTRODUCTION

Mg alloy components are mostly produced through high pressure die-casting.<sup>[1,2]</sup> Alloy development as well as optimisation of casting processes can result in materials of superior mechanical properties, especially at elevated temperatures. The relatively high fraction of porosity due to solidification shrinkage and gas entrapment due to turbulent die filling are some of the main problems

in die-casting and significantly impact the mechanical properties.<sup>[3]</sup>

The basic feature of semisolid processing is the formation of a thixotropic suspension of solid spheres immersed in a liquid matrix.<sup>[4–6]</sup> The generation of the thixotropic slurries is explained in detail elsewhere.<sup>[7]</sup> The rheological properties of the mixture allow the filling of the moulds under laminar flow conditions, which facilitates the use of geometrically complex moulds.

This is an open access article under the terms of the Creative Commons Attribution License, which permits use, distribution and reproduction in any medium, provided the original work is properly cited.

© 2020 The Authors. *Materials and Corrosion* published by WILEY-VCH Verlag GmbH & Co. KGaA, Weinheim

Thixomolding or semisolid metal moulding technology combines conventional die-casting with plastic injection moulding. The process consists of introducing magnesium alloy granules as feedstock in a barrel wherein the granules are heated, thereby raising its temperature while maintaining pressure and shear on it. A large fraction of the material eventually becomes liquid mixed with a portion of primary solid particles under a high shear rate of mixing. The semisolid slurry is then injected into a preheated metal mould to make a net-shape part. Some of the benefits of thixomolding are<sup>[8]</sup>:

- more effective material utilisation through the use of highly complex shape technology;
- high “shot-to-shot” repeatability resulting from a highly automated process;
- close dimensional tolerances on net-shape parts; lower porosity and improved ductility;
- energy savings from the efficient manufacturing cycle;
- extended die life;
- high productivity and potentially lower production costs;
- environment-friendly production (i.e., lowering the impact to global warming by excluding SF<sub>6</sub> cover gas typically used during casting).<sup>[9]</sup>

To date, the effects of the processing parameters such as stirring rate, cooling rate, solid fraction, and temperature have been investigated in depth.<sup>[10–18]</sup>

Regarding the alloy development, the increase of Al concentrations in Mg–Al alloys has a beneficial effect on the corrosion behaviour in chloride media.<sup>[19,20]</sup> The 3 wt% Al content in the AZ31 slightly increased the corrosion resistance, whereas, for the AZ80 and AZ91D alloys, the addition of 8–9 wt% Al significantly increased the corrosion resistance.<sup>[21]</sup> Some authors showed that Al enhances the corrosion resistance of the  $\alpha$ -Mg phase through the formation of an Al-enriched superficial layer,<sup>[22]</sup> which provides better passivation properties than the common Mg(OH)<sub>2</sub> corrosion layer.<sup>[21]</sup> It is also proposed that Al can enhance the protection of the  $\alpha$ -Mg phase through a superficial layer of a carbonate hydroxide of magnesium and aluminium.<sup>[22]</sup>

In Mg–Al alloys, the Al is partly in solid solution and partly precipitated in the form of  $\beta$ -phase, Mg<sub>17</sub>Al<sub>12</sub>, along grain boundaries as a continuous phase as well as part of a lamellar structure.<sup>[23]</sup> An important effect of the Al addition is, thus, the formation of galvanic coupling. Some authors showed<sup>[24,25]</sup> that the galvanic current between the progressively Al-enriched  $\alpha$ -Mg phase and Mg<sub>17</sub>Al<sub>12</sub> increases with the Al content of the  $\alpha$ -Mg solid-solution alloy, whereas contradictory results have been also shown.<sup>[22]</sup> It was shown that the presence of Zn in the  $\alpha$ -Mg phase has no influence on galvanic

corrosion.<sup>[22]</sup> However, those works did not focus on the  $\beta$ -phase size and distribution. The  $\beta$ -phase can act as a galvanic cathode accelerating the corrosion progress when there is a small volume fraction, but at high volume fractions, a barrier effect that inhibits the overall corrosion of the alloy is observed.<sup>[26,27]</sup> Furthermore, it was also reported that the surrounding Al-rich- $\alpha$  or eutectic- $\alpha$  can have approximately 12 wt% Al compared with 1.5 wt% in the grain centre and can strongly define the corrosion behaviour of Mg–Al alloys.<sup>[25,28,29]</sup>

In Mg–Al–Ca (AZC)-based alloys, Mg<sub>2</sub>Ca and/or Al<sub>2</sub>Ca phases are known to form in the interdendritic region in preference to the Mg<sub>17</sub>Al<sub>12</sub> phase observed in the binary system.<sup>[30]</sup> The corrosion rate of AZC alloys decreased with increasing Ca content, especially when the Ca content was more than 1 wt%. The addition of Ca improved the corrosion resistance of AZ91D alloys due to the formation of reticular Al<sub>2</sub>Ca along the grain boundaries.<sup>[31]</sup> In addition, Ca addition combines with Al to form Al<sub>2</sub>Ca phase before the eutectic reaction, which decreases the quantity of eutectic at the grain boundary during solidification.<sup>[32]</sup> Moreover, corrosion potential results indicated that Ca addition reduced susceptibility to breakdown of passive film. X-ray photoelectron spectroscopy measurements showed enrichment of Ca in the oxide layer, indicating an improved formation of a passive film on the surface of AZ91 alloy.<sup>[33]</sup> It was found that increasing the Ca content from 0.9 to 1.8 wt% improves the corrosion resistance of the Mg<sub>5</sub>Al. In this case, Ca addition was attributed to the reduction of the average grain size, increasing the corrosion resistance as the intermetallic compounds located at grain boundaries are more continuous and act as a barrier to the advance of corrosion. The intermetallic compounds contain Al and Ca and are much less cathodic than the  $\beta$ -phase, thus making the microgalvanic effect in the specimen less effective.<sup>[34]</sup>

MRI153 is a casting magnesium alloy, which has been developed based on AZ91 alloy by Dead Sea Magnesium and Volkswagen AG and is used in automotive transmission housing.<sup>[35]</sup> High levels of Al (9 wt%) and Zn (1 wt%) contents improve the alloy's yield strength and castability, while Ca (1 wt%) and Sr (0.1 wt%) are added to form intermetallic phases at grain boundaries and inside the grains to improve creep resistance.<sup>[35]</sup> Zhu et al.<sup>[35]</sup> showed that the microstructure of MRI153 alloy produced via different processes of casting including die-casting, squeeze casting, and ingot casting indicated that the compounds in the interdendritic regions were  $\beta$ -phase and (Mg,Al)<sub>2</sub>Ca phases. Contrary to previous works,<sup>[31]</sup> secondary phases in MRI153 were found to be hexagonal (Mg,Al)<sub>2</sub>Ca and cubic Mg<sub>17</sub>Al<sub>12</sub> phases while the cubic Al<sub>2</sub>Ca phase was not observed.<sup>[36]</sup>

The influence of the casting process on the corrosion behaviour of Mg alloys has been investigated.<sup>[37,38]</sup> Die-cast AM50 showed enhanced corrosion resistance compared with sand and graphite-mould cast.<sup>[37]</sup> A similar behaviour was observed for the AZ91 alloy.<sup>[38]</sup> Die-cast material exhibited a lower corrosion rate and better passivation compared with ingot material. The corrosion resistance of a rheocast AM50 alloy was improved in comparison with the die-cast alloy.<sup>[39]</sup> The corrosion resistance of AZ91D produced via the semisolid processing was higher compared with the same alloy manufactured by high pressure die-casting.<sup>[22,40]</sup> The corrosion resistance in a saline aqueous solution of a rheocast AZ91 alloy was ~15 times higher in comparison with the same alloy produced via gravity cast.<sup>[41]</sup>

It was proposed that the best corrosion resistance observed for semisolid cast specimens is due to a continuous and small meshed Mg<sub>17</sub>Al<sub>12</sub> network, a homogeneous and small  $\alpha$ -Mg grain size, a minimal extent of Al and Zn segregations and higher amount of  $\beta$ -phase in comparison to other production process.<sup>[42,43]</sup> Mathieu et al.<sup>[43]</sup> investigated the corrosion behaviour of high-pressure die-cast and thixocast AZ91D alloys. The better corrosion resistance of the thixocast alloy was attributed to the smaller surface area ratio between cathodic and anodic sites and smaller differences between the Al content of the  $\alpha$ -Mg and  $\beta$ -phase. It was also proposed that the better corrosion resistance of the semisolid alloy cannot be due to the  $\beta$ -phase acting as a barrier, since this phase was present as large discontinuous grains.

To clarify the corrosion mechanism in thixomolded Mg alloy, this study aims to investigate the corrosion behaviour of conventional alloy AZ91D and the experimental alloy MRI153M both produced via thixomolding. First steps of corrosion, electrochemical impedance spectroscopy (EIS) tests, hydrogen evolution, glow discharge optical emission spectroscopy (GDOES), and atomic emission spectroelectrochemistry (AESEC) results are correlated with the chemical composition and microstructure of the investigated alloys.

## 2 | EXPERIMENTAL PROCEDURES

The thixomolding trials were performed at “Neue Materialien Fürth GmbH, Germany” using a thixomolding machine from Japan Steel Works “JLM220MG” with a clamping force of 220 tons. Magnesium granules were fed into a cylinder using a rotating screw. During transport in the cylinder, the magnesium granules were heated up to a semisolid or totally liquid state. At last the

magnesium melt was injected with ram speeds under high pressure into the mould cavity. The die temperature was held at 200°C, the ram speed was 1.8 m/s, and Ar was used as protective gas throughout the experiment. Two Mg alloys, AZ91D and MRI153M, were investigated and their actual chemical composition was measured with X-ray fluorescence (Zn and Ca) and a spark analyser (Al, Sr, Cu, Fe, Si, Ni, and Mn). In our previous work,<sup>[44]</sup> a detailed investigation of the influence of the processing parameters on the corrosion resistance measured by hydrogen evolution was reported. In the present work, the material exhibiting the highest and lowest corrosion rates from this previous work<sup>[44]</sup> is investigated in detail, aiming to clarify the enhanced corrosion resistance of these alloys and the difference in corrosion resistance between the thixomolded AZ91D and MRI153M. The processing parameters that were used in the current investigation are listed in Table 1.

Specimens for metallographic characterisation were ground with SiC abrasive papers from P500 to P2500 followed by polishing using silica oxide polishing suspension (OPS). The specimens for optical microscopy (OM) were etched with an acetic-picric solution,<sup>[45]</sup> and OM was performed with a Leica DMI 5000 reflected light microscope using polarised light to set up Normanski contrast to determine the grain sizes. The latter was determined according to the ASTM standard E112-12<sup>[46]</sup> using the linear intercept method. Scanning electron microscopy (SEM) was conducted on the unetched samples using a Carl Zeiss FEG-SEM Ultra 55 and a Tescan Vega3 SEM. Stereological measurements were performed by using a minimum of 10 random back-scattered electron (BSE) macrographs to determine the area fraction of porosity and of intermetallic compounds. The images were analysed using ImageJ software.

Phase characterisation of the as-cast specimens was conducted with synchrotron radiation diffraction using the facilities of P07 beamline of Petra III, Deutsches Elektronen-Synchrotron. A monochromatic beam with energy of 100 keV ( $\lambda = 0.0124$  nm) and with a cross-section of 1.0 mm  $\times$  1.0 mm was used. Diffraction patterns were recorded with a PerkinElmer 1622 flat panel detector with a pixel size of (200  $\mu\text{m}^2$ ), which was placed at a sample-to-detector distance of 1,535 mm from the specimen (calibrated with a LaB<sub>6</sub> standard powder

**TABLE 1** Processing parameters for the thixomolding trials for the production of the AZ91D and MRI153M alloys

Alloy	Solid content (%)	Injection temperature (°C)	Thickest of the part (mm)
AZ91D	20–30	585	2
MRI153M	3–5	600	14

sample). The Pearson crystallographic database<sup>[47]</sup> was used to obtain the information of possible phases and CaRIne crystallographic software<sup>[48]</sup> was used to simulate the theoretical diffraction patterns for various phases.

The corrosion resistance was investigated via hydrogen evolution.<sup>[49,50]</sup> Hydrogen evolution tests were performed using eudiometers, art. nr. 2591-10-500 from Neubert-Glas, Germany; for a more detailed description of eudiometers, see Lamaka et al.<sup>[51]</sup> From AZ91D, specimens with 20 mm length, 20 mm width, and 1.5 mm thickness (surface area, 8.6 cm<sup>2</sup>) were prepared by grinding with SiC abrasive papers from P500 to P2500. From MRI153M, specimens with 14 mm length, 14 mm width, and 12 mm thickness (surface area, 10.6 cm<sup>2</sup>) were prepared using the same procedure as adopted for the AZ91D. The measurements were performed in 5.0 wt% NaCl naturally aerated pH neutral solution for up to 21 days. A minimum of three specimens were tested for each condition.

Degradation behaviour was studied by additional immersion tests in 5.0 wt% NaCl naturally aerated pH neutral solution after 1 day and 7 days. Those specimens were prepared by grinding with SiC abrasive paper up to P2500 followed by polishing with OPS. The corrosion products were removed by pickling in a solution containing 200 g/L CrO<sub>3</sub> at room temperature for 5–10 min following the ASTM standard G1-90, Designation C5.2. The cleaned surface was investigated with a Tescan Vega3 SEM using BSE and SE electron mode operating at 15 kV. The results were correlated with corrosion behaviour.

Electrochemical tests were conducted in a stirred aqueous 5.0 wt% NaCl solution at 22 ± 0.5°C using a Gill AC computer-controlled potentiostat. A typical three-electrode cell with the specimen as the working electrode (0.5 cm<sup>2</sup> exposed area), a saturated Ag/AgCl electrode as the reference electrode, and a platinum mesh as a counter electrode were used. EIS measurements were performed for immersion times ranging from 1 hr to 7 days at room temperature. The frequency range was from 0.01 Hz to 30 kHz and the amplitude of the sinusoidal potential signal was 10 mV with respect to the open-circuit potential (OCP).

GDOES analysis was performed with GD-Profilier 2 (HORIBA Jobin Yvon) using the Quantum software. The instrument configuration included a pulsed radiofrequency (RF) generator, a standard HJY glow discharge source with an anode of 4-mm internal diameter, and an automatic impedance matching system between the RF generator and the GD source. Ar/H<sub>2</sub> (10,000 ppm H<sub>2</sub>) mixture supplied by Air Liquide was employed as the discharge gas. The differential interferometry profiling system integrated in the instrument allowed a direct

depth measurement along with the elemental depth profile analysis; 750 Pa and constant power of 17 W were utilised. Specimens of thixomolded AZ91D with 20 mm length, 20 mm width and 1.5 mm thickness were prepared by grinding with SiC abrasive papers followed by polishing in OPS suspension. Specimens of MRI153M with 14 mm length, 14 mm width, and 12 mm thickness were prepared using the same procedure as adopted for the AZ91D. The samples were immersed in 1 wt% NaCl for 3 days. The spectral wavelengths used for detection were Mg, 285 nm; Al, 396 nm; Mn, 258 nm; Ca, 423 nm; Zn, 481 nm; and O, 130 nm. The emission signals of 47 elements were recorded but only the signals of the species of interest are discussed in the paper.

Online measurement of partial elements dissolution was performed by means of AESEC technique described elsewhere.<sup>[52]</sup> Briefly, it consists of an electrochemical flow cell connected with an inductively coupled plasma atomic emission spectrometer (ICP-AES). In the flow cell, a reaction between the sample and an electrolyte (1 wt% NaCl) occurs, leading to the production of dissolved cations and/or slightly soluble species. Then, the electrolyte is transported downstream to the ICP-AES, where its composition is continuously analysed. The ICP-AES analysis shows only the concentrations of the released species present in a soluble form, while the low soluble products or surface films cannot be directly detected. The samples were in contact with the flowing solution at OCP within 5 min; then the anodic potential  $E = 1$  Vvs. OCP was applied for 18 min. The average concentration of the released species was calculated for the steady-state period (the last 5 min of anodic polarisation), when all the signals were stable. Ca dissolution was not uniform; the results obtained in the first 3 min of anodic polarisation (initial period) and the last 5 min (steady-state period) are presented.

### 3 | RESULTS AND DISCUSSION

Table 2 exhibits the measured chemical composition for the thixomolded AZ91D and MRI153M alloys. It is important to highlight the low impurity level of both alloys. Moreover, the Al, Mn, Zn, and Si contents were comparable between the two investigated alloys. The MRI153M alloy can be considered as a modified AZ91D with Ca and Sr additions (in the current case, 0.9 and 0.1 wt%, respectively).

The solidified melt of the AZ91D alloy produced by thixomolding process formed four different solid constituents: primary  $\alpha$ -Mg grains, secondary  $\alpha$ -Mg grains, and eutectic consisting of tertiary  $\alpha$ -Mg and  $\beta$ -phase (Mg<sub>17</sub>Al<sub>12</sub>) and other phases of minor volume fraction.

**TABLE 2** Measured chemical composition of the investigated AZ91D and MRI153M produced via thixomolding

Chemical composition (wt%)										
Alloy	Al	Mn	Zn	Si	Cu	Ni	Fe	Ca	Sr	Mg
AZ91D	8.73	0.24	0.77	0.01	0.002	0.0006	0.0014	–	–	Balance
MRI153M	8.93	0.31	0.67	0.01	0.001	0.0008	0.0023	0.90	0.10	Balance

The primary  $\alpha$ -Mg grains are formed in the barrel. They are globular in shape because dendrite arms are broken due to high shear stresses in the melt that act continuously as long as the feedstock is transported in the barrel.<sup>[53]</sup>

The OM and SEM–BSE micrographs are shown in Figure 1. Figure 1a,b show the typical microstructure of the AZ91D and MRI153M, respectively. In the case of the AZ91D, the typical microstructure was characterised by a matrix of fine globular secondary  $\alpha$ -Mg grains with coarse primary  $\alpha$ -Mg immersed in the matrix. For the AZ91D, it is notable the presence of coarse primary  $\alpha$ -Mg globular grains. The MRI153M also exhibits similar morphology, and the main difference was the presence of coarser secondary  $\alpha$ -Mg grains in comparison to the AZ91D. As explained in our previous publication,<sup>[44]</sup> this is mainly attributed to the processing parameters adopted for each alloy. The thickness of the region from where the specimens of MRI153M was extracted is three times higher compared with the AZ91D. Moreover, the lower solid content that was used during the injection of the MRI153M implies in higher solidification time compared with the AZ91D, which leads to higher grain size. Other phases were found at the grain boundaries, such as

$\text{Al}_{12}\text{Mg}_{17}$  (in both alloys), particles containing mainly Al (~60 at%), Mn (~35 at%) and Ca and Zn (~5 at%) indexed according to the  $\text{Al}_8\text{Mn}_5$  structure (in both alloys),  $\text{Al}_2\text{Ca}$  (in the case of the MRI153M) and minor impurities (in both alloys). The  $\text{Al}_8\text{Mn}_5$  particles are larger for the MRI153M compared with the AZ91D. No notable trace of Mn was found within the  $\alpha$ -phase, as was also observed in Zander and Schnatterer.<sup>[42]</sup> In this way, among the identified phases, the main difference between the AZ91D and MRI153M is the presence of small particles of  $\text{Al}_2\text{Ca}$  at the grain boundaries. EDXS point analysis (not shown here) indicated that the presence of Ca in the  $\text{Al}_{12}\text{Mg}_{17}$  and the Al–Mn particles are neglectable. The notable small volume fraction of this phase suggests that Ca was also present in small amounts as a solid solution especially in the secondary  $\alpha$ -Mg matrix. Czerwinski and Zielinska-Lipiec<sup>[54]</sup> showed that for the addition of 2 wt% Sr to a Mg–5Al alloy,  $\text{Al}_4\text{Sr}$  or  $\text{Mg}_{17}\text{Sr}_2$  are found in the microstructure. In the present investigation, no traces of such phases are observed.

Some level of porosity is also present in both materials, indicating that gases were entrapped into the solidifying material during metal injection. Figure 1c,d exhibit the distribution of intermetallic compounds for

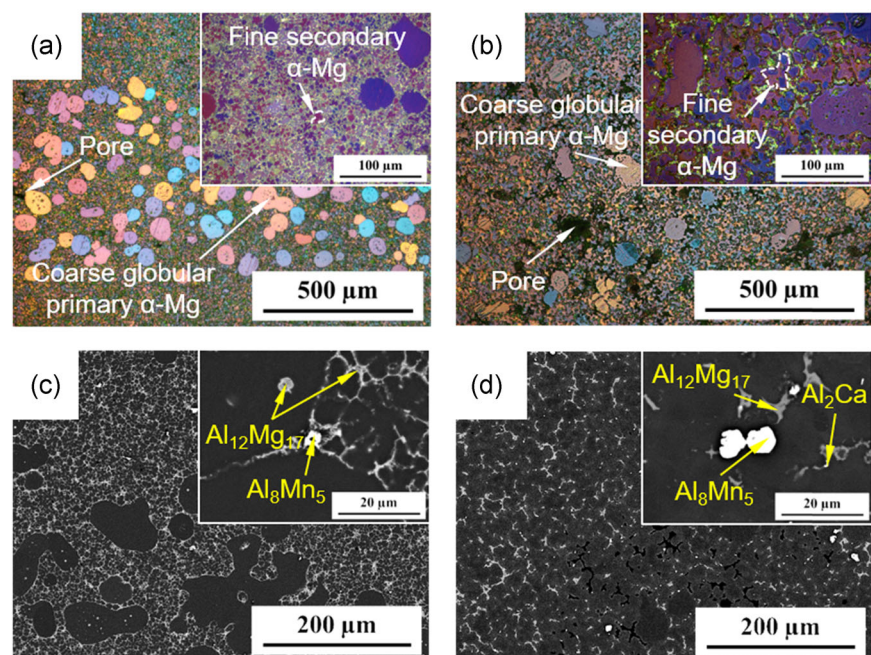


**FIGURE 1** Optical micrographs (a and b) and scanning electron microscopy–backscattered electron micrographs (c and d) of the thixomolded AZ91D (a and c) and MRI153M (b and d) [Color figure can be viewed at [wileyonlinelibrary.com](http://wileyonlinelibrary.com)]



both alloys. Some of the coarse primary  $\alpha$ -Mg grains exhibited some droplets of the intermetallic compound inside. This suggests that they had liquid inside when injected into the mould as explained by Zhang et al.<sup>[55]</sup> The MRI153M, though, exhibits a smaller difference in grain size between the primary and secondary  $\alpha$ -Mg, impacting the distribution of intermetallic compounds along the grain boundaries. In the case of the MRI153M, the network of intermetallic compounds along the grain boundary seems to be less continuous compared with the AZ91D. The smaller grain size of the secondary  $\alpha$ -Mg is related to a larger volumetric density of grain boundary. In a first approach that would prevent the second phases to be spread continuously along grain boundaries. However, the injected liquid fraction has higher concentration of Al for AZ91D compared with MRI153M because of the significantly higher volume fraction of primary  $\alpha$ -Mg grains. Thus, an increase in the volume fraction of the second phases thus a continuous phase along grain boundaries is observed.<sup>[34]</sup> Moreover, the Al-Mn particles were notable coarser in the case of the MRI153M compared with the AZ91D, as highlighted in the insert in Figure 1d.

The first  $\alpha$ -Mg matrix to be formed during solidification has the lowest Al content when compared with the following formed  $\alpha$ -Mg matrix. When the material is injected into the mould, the primary globular  $\alpha$ -Mg is expected to exhibit lower Al content compared with the secondary  $\alpha$ -Mg. Moreover, the outer regions of the secondary  $\alpha$ -Mg grains are supersaturated with Al because of enrichment of the liquid phase with Al during solidification. Even though the Al content in the primary  $\alpha$ -Mg is lower compared with the secondary  $\alpha$ -Mg grains, the  $\alpha$ -Mg can contain at least 3 wt% Al as demonstrated for a semisolid processed AZ91 alloy.<sup>[22]</sup> This value is notably higher compared with a die case DC alloy ( $\alpha$ -Mg contains only 1.8 wt% Al).<sup>[22]</sup>

Table 3 summarises the microstructure features of the two investigated alloys. The grain size in both coarse primary and fine secondary  $\alpha$ -Mg grains is higher for the MRI153M compared with the AZ91D. Porosity is also higher for the MRI153M compared with the AZ91D. The contents of  $\beta$ -phase and other particles are slightly higher for the MRI153M compared with the AZ91D. However,

**TABLE 4** Indexed phases for the AZ91D and MRI153M alloys produced by thixomolding

Phase	AZ91D	MRI153M
$\alpha$ -Mg	Present	Present
$\text{Al}_{12}\text{Mg}_{17}$ ( $\beta$ -phase)	Present	Present
$\text{Al}_8\text{Mn}_5$	Low amount	Low amount
$\text{Al}_2\text{Ca}$	Not present	Very low amount
$\text{Al}_{11}\text{Ce}_3$	Not present	Very low amount

the measurement method that was applied does not provide sufficient accuracy.

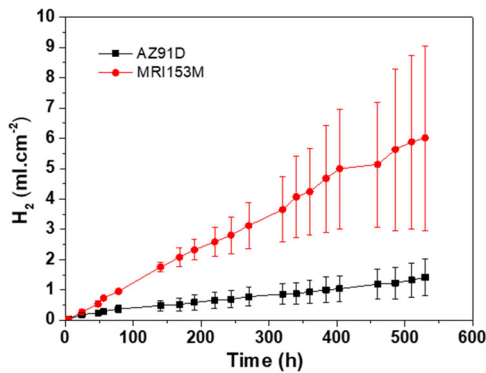
Complementary to Table 3, Table 4 shows that the only difference in the present phases relies on the small fraction of  $\text{Al}_{11}\text{Ce}_3$  (due to very small rare earth [RE] additions) and  $\text{Al}_2\text{Ca}$ , that were identified for the MRI153M but not for the AZ91D alloy.  $\text{Al}_{12}\text{Mg}_{17}$  is the  $\beta$ -phase. The Ce (and other RE elements) content is not exhibited in the measured chemical composition (Table 2) since it does not belong to the nominal composition of the MRI153M alloy. As reported in the literature,  $\text{Al}_2\text{Ca}$  intermetallic compounds formed in the microstructure instead of  $\text{Mg}_2\text{Ca}$ .<sup>[56]</sup>

Figure 2 exhibits the hydrogen evolution plots for the investigated alloys. The AZ91D exhibited notable higher corrosion resistance compared with the MRI153M. The standard deviation increases with immersion time. This can be attributed to the high porosity and the heterogeneity in pore size and distribution from sample to sample. As explained in the experimental procedures section, the external area of each sample was measured before immersion. However, when pores are present, the real area that is in contact with the electrolyte is larger compared with the calculated one.

Table 5 shows the corrosion rates measured with hydrogen evolution using 5.0 wt% NaCl solution. The thixomolded AZ91D exhibited the lowest values of corrosion rate. For short immersion times the corrosion rate of AZ91D was comparable with MRI153M. However, for longer immersion times, the corrosion rate of AZ91D was approximately 4–5 times lower compared with MRI153M. The measured corrosion rates reported in this study are significantly lower compared with the other

**TABLE 3** Grain size, area fraction of porosity,  $\beta$ -phase, and other phases for the thixomolded AZ91D and MRI153M alloys

Alloy	Grain size ( $\mu\text{m}$ )	Porosity (%)	$\beta$ -Phase (%)	Other phases (%)	
AZ91D	Coarse primary $\alpha$ -Mg	$66.6 \pm 16.6$	$4.6 \pm 1.5$	$6.0 \pm 0.5$	$0.3 \pm 0.1$
	Fine secondary $\alpha$ -Mg	$6.7 \pm 0.2$			
MRI153M	Coarse primary $\alpha$ -Mg	$81.7 \pm 14.2$	$7.8 \pm 2.6$	$6.7 \pm 0.9$	$0.6 \pm 0.1$
	Fine secondary $\alpha$ -Mg	$9.9 \pm 0.2$			



**FIGURE 2** Normalized hydrogen evolution curves in stirred 5.0 wt% NaCl solution for the investigated thixomolded alloys [Color figure can be viewed at wileyonlinelibrary.com]

works.<sup>[27,38,57,58]</sup> Ambat et al.<sup>[38]</sup> reported that die-cast AZ91D exhibited corrosion rates higher than 2 mm/year in 3.5 wt% NaCl media, and ingot-cast AZ91D higher than 3 mm/year. Thus, the AZ91D and MRI153M produced by thixomolding and investigated in the present work exhibit superior corrosion resistance compared with other production methods, especially taking into account that more concentrated NaCl electrolyte was used in our tests.

EIS was also performed to assess the corrosion resistance of the investigated alloys and the results for 1 and 7 days are shown in Figure 3a,b as Nyquist and Bode plots, respectively. The Nyquist plots show a capacitive semicircle at high and intermediate frequencies, which can be attributed to the charge transfer reaction during the Mg corrosion process. An inductive loop was also observed and is attributed to the porosity and instabilities of the system.<sup>[59]</sup> The estimated resistance values from the diameter of the semicircles of the Nyquist plots (Figure 3a) of the AZ91D is approximately  $1,000 \Omega \cdot \text{cm}^2$  after 1-day immersion and approximately  $1,300 \Omega \cdot \text{cm}^2$  after 7 days immersion. For the MRI153M the estimated resistance values were approximately  $550 \Omega \cdot \text{cm}^2$  after 1 day immersion and approximately  $750 \Omega \cdot \text{cm}^2$  after 7 days immersion. The increase of the resistance values from 1 to 7 days immersion can be attributed to the increase in the thickness of the corrosion products, Figure 3c. The

**TABLE 5** Corrosion rates obtained from hydrogen evolution tests using 5.0 wt% NaCl solution

Immersion time	Corrosion rates (mm/year)	
	AZ91D	MRI153M
1 Day	$0.44 \pm 0.13$	$0.65 \pm 0.21$
1 Week	$0.17 \pm 0.07$	$0.68 \pm 0.12$
3 Weeks	$0.14 \pm 0.06$	$0.63 \pm 0.38$

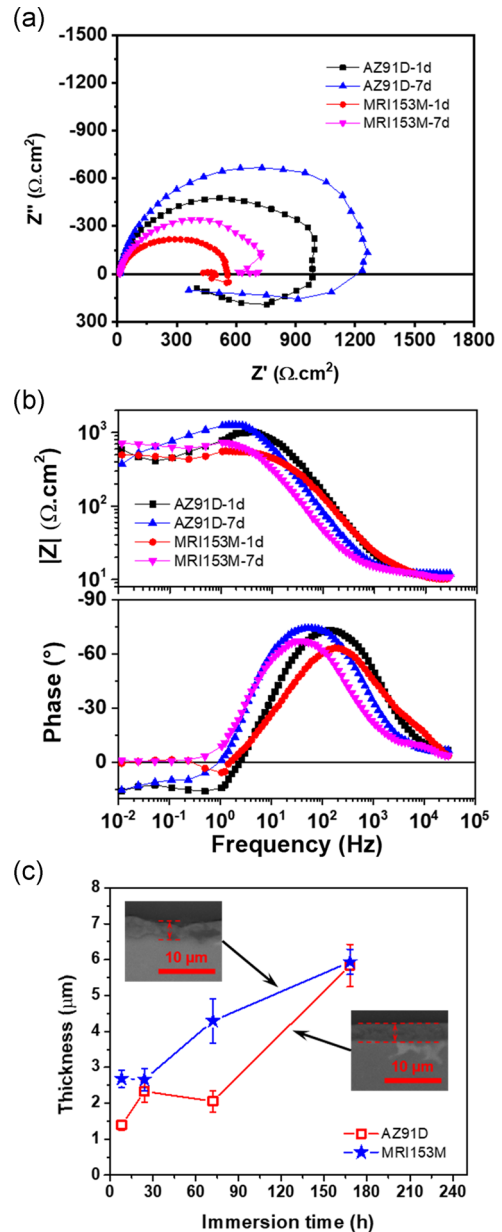


**FIGURE 3** Electrochemical impedance spectroscopy results after immersion in 5.0 wt% stirred solution for the investigated thixomolded alloys (a and b) and thickness evolution of the corrosion products layer for the thixomolded AZ91D and MRI153M alloys (c). (a) Nyquist plots for 1 day and 7 days immersion and (b) Bode plots after 1 day and 7 days immersion [Color figure can be viewed at wileyonlinelibrary.com]

thickness of the corrosion products increased with increasing immersion time and was measured as indicated in inserts in Figure 3c.

Figure 4 exhibits the corroded surface of the investigated alloys after 1 day (a, d) and 7 (b, e) days immersion. The red circles indicate the coarse primary globular  $\alpha$ -Mg grains. The arrows indicate the probable pathway for the corrosion front propagation. It is observed that the corrosion that occurs in the fine secondary  $\alpha$ -Mg globular grains acts as a pathway for the propagation of the

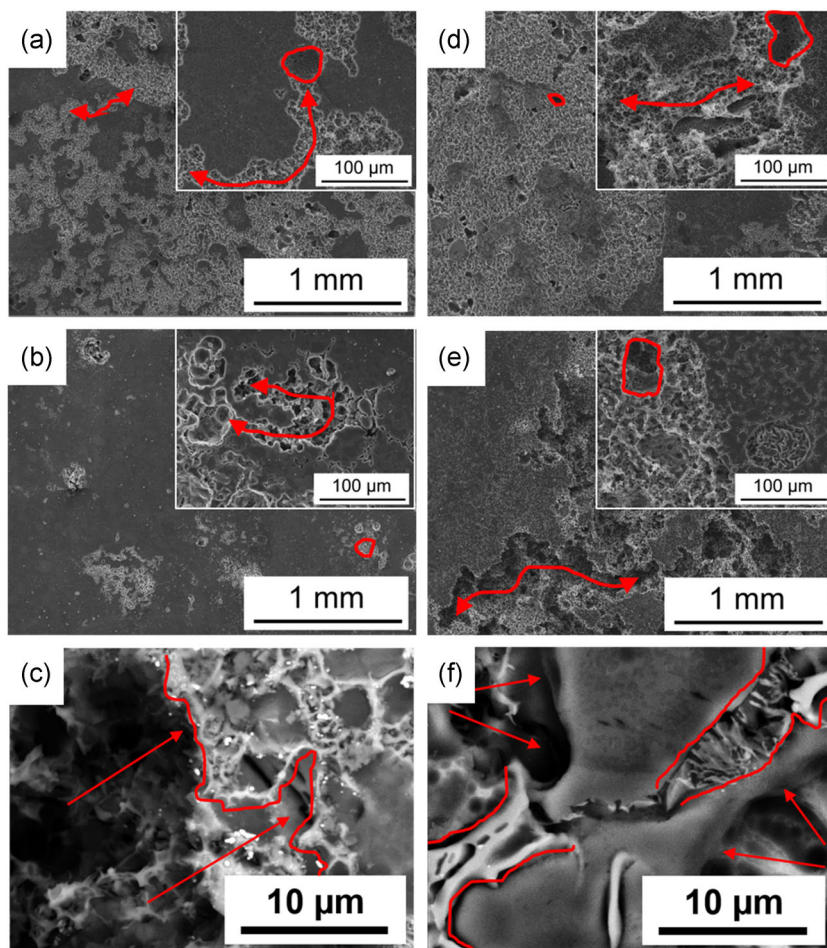


**FIGURE 4** Scanning electron microscopy micrographs of the alloy surface after cleaning with chromic acid for AZ91D (a–c) and MRI153M (d–f) immersed in natural aerated 5.0 wt% NaCl solution; (a and d) 1-day immersion, (b–e) 7 days immersion. Red circles indicate the coarse primary  $\alpha$ -Mg globular grains that corroded. The red arrows in a–f indicate the pathway of the corrosion front propagation [Color figure can be viewed at [wileyonlinelibrary.com](http://wileyonlinelibrary.com)]

localised corrosion, that tends to spread on the surface of the sample. Some intensive localised corrosion regions normally were found to contain coarse globular primary  $\alpha$ -Mg. Figure 4a,d clearly show that already after 1-day immersion, the corrosion propagated consuming the coarse primary globular  $\alpha$ -Mg grains and followed one or more pathways in the region of the fine secondary globular  $\alpha$ -Mg grains. After 7 days immersion, the behaviour is similar, and the coarse primary globular  $\alpha$ -Mg grains are dissolved leaving between them pathways in the fine secondary globular  $\alpha$ -Mg grain region. It is notable, though, that the depth of the pathways is higher after 7 days immersion when compared with that of after 1-day immersion. For the MRI153M, this process leads to regions of intensive localised corrosion. Complementary, Figures 4c and 4f exhibit BSE-SEM micrographs with a lower view field of the corroded areas of the AZ91D and MRI153M, respectively. It can be observed that the  $\text{Al}_{12}\text{Mg}_{17}$  did not dissolve, as expected since they are cathodic with respect to the matrix. It has been shown that for a AZ91 alloy produced by rheocasting, the early stages of corrosion were located at the centre of  $\alpha$ -Mg globules and more importantly at  $\alpha$ -Mg/ $\beta$ -phase interfaces due to galvanic coupling.<sup>[41]</sup> Regarding galvanic coupling,

corrosion around  $\text{MnAl}_2$  inclusions is also reported to play a role in Mg–Al alloys.<sup>[60]</sup>

Czerwinski et al.<sup>[61]</sup> investigated the existence of chemical segregation within the primary grains. Traces of Al and Zn below the detection level are found in the centre of the grains. On the other hand, the content of Al and Zn increases while moving towards the interface with the intermetallic phase as also shown in Tissier et al.<sup>[62]</sup> It was observed that the interface between the primary  $\alpha$ -Mg grains and the eutectic has an irregular shape. Numerous protrusions of intermetallic compounds cover the well-developed interface. Transmission electron microscopy investigations also showed pile up of dislocations against the  $\alpha$ -Mg grain boundary.<sup>[61]</sup>

For the investigated thixomolded alloys, it is proposed that a combination of microstructural features is responsible for their corrosion behaviour. Figure 5 exhibits schematically the proposed corrosion pathway for the investigated thixomolded alloys. It is observed in Figure 4 that the coarse primary  $\alpha$ -Mg grains are intensively corroded. As already discussed, during solidification of the thixomolded material, the coarse primary  $\alpha$ -Mg (Region A) exhibits lower Al content (and hence less protective oxide) compared with the fine secondary  $\alpha$ -Mg



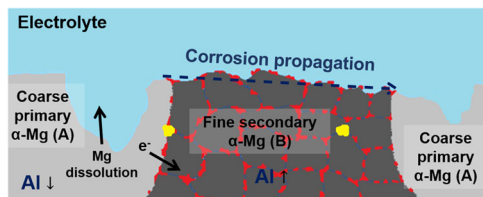


**FIGURE 5** Schematic representation of the proposed corrosion processes that take place for the investigated thixomolded AZ91D and MRI153M alloys. The red regions indicate the  $\text{Al}_{12}\text{Mg}_{17}$  ( $\beta$ -phase) and the yellow ones represent the other phases that are present in the material or inclusion particles [Color figure can be viewed at [wileyonlinelibrary.com](http://wileyonlinelibrary.com)]

(Region B),  $\text{Al}_{(A)} < \text{Al}_{(B)}$ . In this case, Region B acts as cathodic areas with respect to Region A, explaining the intensive corrosion of the coarse primary  $\alpha$ -Mg grains-A. For the investigated thixomolded alloys, it is proposed that the difference in Al content between Regions A and B acts as the main driving force for corrosion propagation. The volume fraction of coarse primary  $\alpha$ -Mg for the AZ91D is significantly higher compared with the MRI153M. Therefore, it is proposed that other localised corrosion mechanisms play a more important role for the MRI153M, rather than for the AZ91D. Therefore, the presence of cathodic and anodic regions (Region B/Region A) is the major mechanism for corrosion of a thixomolded alloy. For a die-cast alloy, there is no fine secondary  $\alpha$ -Mg nor coarse primary  $\alpha$ -Mg. In this case, there are only fine grains with similar Al contents, that might exhibit microsegregation in the interior of the grain. Moreover, the Al content in the  $\alpha$ -Mg matrix of a die-cast alloy is lower compared with a thixomolded alloy. In the extreme, the ingot-cast material normally exhibits even higher microsegregation compared with a die-cast alloy as well as higher volume fraction of intermetallic compounds that act as sources of galvanic coupling, enhancing the  $\alpha$ -Mg dissolution. Thus, it seems that the presence of the galvanic couple consisted of fine secondary  $\alpha$ -Mg and coarse primary  $\alpha$ -Mg acting as driving force for  $\alpha$ -Mg dissolution is less detrimental to the corrosion resistance of Mg–Al alloys in comparison to the presence of microsegregation within a grain and intermetallic compounds acting as sources of galvanic coupling.

Porosity also play a role on the corrosion resistance, enlarging the reactive surface of the metal and affecting the formation of autocatalytic cells. Both aspects increase the corrosion rate and therefore, porosity is always detrimental for corrosion resistance.<sup>[58]</sup> However, our previous work<sup>[44]</sup> shows that porosity seems to be a factor of minor relevance when compared with the other microstructural aspects in accordance to Zander and Schnatterer.<sup>[42]</sup> In this study, porosity is attributed to increase slightly the corrosion rate of the investigated

materials, but it is not the prevailing corrosion mechanism that explains the difference of the corrosion resistance between MRI153M and AZ91D alloys.

Impurities, microgalvanic cells and segregation can create local sites of  $\alpha$ -Mg dissolution, degenerating eventually the corrosion resistance of the material. The presence of the  $\text{Al}_{12}\text{Mg}_{17}$  as well as the intermetallic particles containing Mn ( $\text{Al}_8\text{Mn}_5$  for both alloys) or Ca/RE (for the MRI153M) also play an important role on the propagation of the corrosion front in Region B. Figure 4 indicates that there is a preferential pathway for corrosion propagation, so that the corrosion front tends to consume the fine secondary  $\alpha$ -Mg grains connecting the multiple coarse primary  $\alpha$ -Mg grains. Figures 4c and 4f, show that the  $\text{Al}_{12}\text{Mg}_{17}$  phase remained in the microstructure while the  $\alpha$ -Mg corroded (as indicated by the red arrows). The network of  $\beta$ -phase along the secondary fine  $\alpha$ -Mg grains is not continuous for the AZ91 nor for the MRI153M, Figure 1c,d, respectively. In this case, it could be expected that the higher the volume fraction of  $\beta$ -phase, the higher the corrosion due to microgalvanic cell formation. However, the AZ91 alloy exhibits a significantly higher corrosion resistance compared with the MRI153M and both alloys exhibit comparable volume fraction of  $\beta$ -phase. The network of the  $\beta$ -phase seems to be significantly better interconnected for the AZ91D compared with the MRI153M. In Figure 4c the dissolution of  $\alpha$ -Mg seems to be partially hindered by the presence of this network of  $\beta$ -phase. On the other hand, the role as barrier to the dissolution of  $\alpha$ -Mg seems to be neglectable for the MRI153M since the  $\text{Al}_{12}\text{Mg}_{17}$  particles are sparsely distributed along the grain boundaries. This effect can be seen in Figure 4f by a relatively higher dissolution of the  $\alpha$ -Mg at the grain boundaries compared with its vicinity.

However, the difference in the  $\alpha$ -Mg matrix or the different volume fractions and distribution of  $\beta$ -phase are not the only difference between the AZ91D and the MRI153M alloys. The minor additions of Sr and RE and especially the presence of Ca also play a role. Figure 4 indicates that the depth of the pathway in Region B was notably higher for the MRI153M compared with the AZ91D alloy. Three possible phenomena are competing in this case: The dissolution of  $\alpha$ -Mg was facilitated by the presence of microgalvanic corrosion; corrosion due to segregation between the centre of the fine secondary  $\alpha$ -grains and the vicinity of the grain boundary played a role; or the corrosion front advance was hindered in the case of the AZ91D but not in the case of the MRI153M.

To clarify these abovementioned hypotheses, the elemental depth profiling of the AZ91D and MRI153M alloys after 3 days immersion in 1% NaCl solution was performed by GDOES. Figure 6 demonstrates the

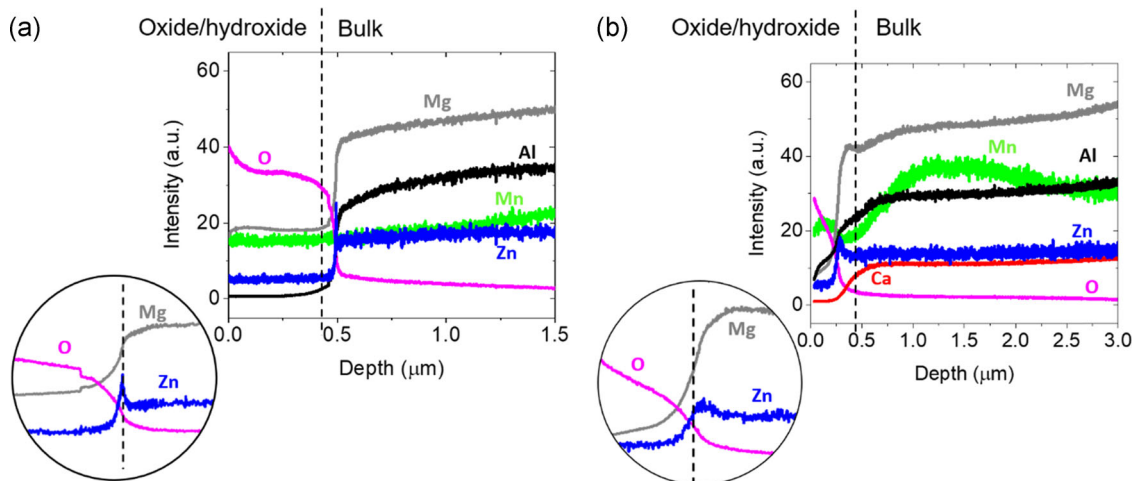


**FIGURE 6** Results of glow discharge optical emission spectroscopy equipped with a differential interferometry profiling. Samples were immersed in 1 wt% NaCl solution for 3 days [Color figure can be viewed at [wileyonlinelibrary.com](http://wileyonlinelibrary.com)]

qualitative profiles, first, the corrosion products are analysed till the element intensity reaches a stable level (i.e., it corresponds to the bulk). Figure 6a shows the GDOES results for the thixomolded AZ91D alloy. Al is not present in the oxide layer in the AZ91D. In addition, an enrichment of Zn on the interface oxide/bulk and no variation of Mn in the bulk are observed. The GDOES results for the thixomolded MRI153M is shown in Figure 6b. Contrary to AZ91D, a small concentration of Al is found in the MRI153M. Moreover, a notable variation of Mn is observed in the bulk. The  $Al_8Mn_5$  particles present in the MRI153M are notable larger compared with AZ91D. Moreover, their distribution is sparser in the MRI153M compared with AZ91D, which can explain the local variation of Mn in the MRI153M. As observed in the AZ91D, an enrichment of Zn on the interface oxide/bulk is also present in the MRI153M. Ca is not observed in the oxide layer in the MRI153M. It is reported that the enrichment of Ca in the oxide layer can

enhance the corrosion resistance of Mg alloys.<sup>[33]</sup> However, that effect is absent in the investigated thixomolded MRI153M. The absence of Al in AZ91D and very low concentration in MRI153M in the oxide layer agrees with the immersion tests results, which show that the  $Al_{12}Mg_{17}$  remains at the microstructure during corrosion (Figure 4). Moreover, the formation of an Al-enriched superficial layer as responsible for the enhancement of corrosion resistance of AZ91<sup>[22]</sup> has to be neglected in our investigation.

Table 6 exhibits the results of AESEC analysis for the AZ91D and MRI153M alloys. The normalised element fraction with respect to the Mg content provides unique information of how the alloys corroded under anodic polarisation of 1 V. The results show that preferential anodic dissolution of Ca occurs. Ca was found with the  $\alpha$ -Mg and mainly as  $Al_2Ca$  particles at the grain boundaries. Ca is lower in the standard electrode potential compared with Mg and Al,<sup>[63]</sup> which suggest

**TABLE 6** Fraction of dissolved elements measured using AESEC and compared with the measured chemical composition of the thixomolded AZ91D and MRI153M alloys

	Measured composition		Dissolved via AESEC		Mg-normalised fractions ( $C_x/C_{Mg}$ )			
	AZ91D	MRI153M	AZ91D	MRI153M	AZ91D		MRI153M	
	(wt%)	(wt%)	(ppm) (AESEC)	(ppm) (AESEC)	Expected	Measured	Expected	Measured
Ca-initial	0.0016	1.51	0.0000	0.5	0.0000	0.0000	0.0171	0.0250
Ca-steady state	0.0016	1.51	0.0000	0.27	0.0000	0.0000	0.0171	0.0135
Al	8.98	8.81	2.5000	1.25	0.0999	0.1042	0.0995	0.0625
Zn	0.91	0.85	0.0200	0.015	0.0101	0.0008	0.0096	0.0008
Mn	0.25	0.31	0.0000	0.07	0.0028	0.0000	0.0035	0.0035
Mg	89.86	88.52	24.0000	20	1.0000	1.0000	1.0000	1.0000

Abbreviation: AESEC, atomic emission spectroelectrochemistry.

that preferential dissolution of the  $\text{Al}_2\text{Ca}$  particles could occur. It seems to be contradictory with the literature, but in the current case, the  $\text{Al}_2\text{Ca}$  particles are not replacing the  $\beta$ -phase formed during solidification. In fact, the  $\text{Al}_2\text{Ca}$  particles are barely observed in the microstructure. Moreover, in Nam et al.<sup>[33]</sup> it was shown that the presence of Ca in the corrosion products seems to form a better adherent and stable layer. In the current investigation, Ca was not observed in the corrosion layer of the MRI153M (Figure 6b). The corrosion of the regions around the grain boundary (Figure 4f) could be also explained due to dissolution of Ca atoms that should segregate in the regions that are solidified last. This result reinforces the results of the immersion tests, in which the particles containing Ca would dissolve first, leaving a local pathway for the propagation of the corrosion front throughout the grain boundary. Therefore, the mechanism effect of Ca on a Mg–Al thixomolded alloy might differ compared with a die-cast or ingot-cast alloy, in which a bimodal microstructure is not present.

The comparable amount of expected and measured amount of Al content for the AZ91D suggests that this alloy probably was dissolved near homogeneously under anodic polarisation of 1 V. If localised dissolution of Mg occurs, the  $\text{Al}_{12}\text{Mg}_{17}$  particles are expected to remain in the microstructure and the measured Al content would be lower compared with the expected one. This behaviour, though, was observed for the MRI153M alloy. The absence of Mn measured for the AZ91D reveals the scarceness of the Mn-enriched particles in its microstructure. The very low dissolution of Zn under anodic polarisation was unexpected and reveals that regions enriched with Zn tend to suffer low dissolution under anodic polarisation of 1 V. For the AZ91D and MRI153M,

the Zn was found to be distributed in the  $\alpha$ -Mg matrix and also in low content in the  $\text{Al}_{12}\text{Mg}_{17}$  phase as a substitutional element of Al ( $\text{Al,Zn})_{12}\text{Mg}_{17}$ .<sup>[61]</sup> Thus, apart from the selective dissolution of Ca from the MRI153M, the AESEC results show that under anodic polarisation of 1 V, the dissolution of the  $\beta$ -phase for AZ91D should be more general, whereas the site with localised dissolution of the  $\alpha$ -Mg matrix is expected for the MRI153M.

## 4 | SUMMARY AND CONCLUSIONS

First steps of corrosion, EIS tests, hydrogen evolution, GDOES, and AESEC results are correlated with the chemical composition and microstructure of AZ91D and a MRI153M alloy both produced via thixomolding.

In both cases, a bimodal microstructure is observed and it consists of a matrix of fine secondary  $\alpha$ -Mg and coarse globular primary  $\alpha$ -Mg immersed in the matrix. The grain size in both coarse primary and fine secondary  $\alpha$ -Mg grains is higher for MRI153M compared with AZ91D. Porosity is observed and is higher for MRI153M compared with AZ91D. The  $\beta$ -phase ( $\text{Al}_{12}\text{Mg}_{17}$ ) is present in both alloys along the grain boundaries. Particles containing mainly Al and Mn, and indexed as  $\text{Al}_8\text{Mn}_5$  are also observed in both alloys. Fine  $\text{Al}_2\text{Ca}$  particles are observed in MRI153M. The presence of Ca in the  $\text{Al}_{12}\text{Mg}_{17}$  and the Al–Mn particles are neglectable for MRI153M. The fraction of  $\beta$ -phase and other particles are slightly higher for the MRI153M compared with the AZ91D.

The corrosion rates exhibited by the thixomolded AZ91D were at least five times lower compared with AZ91D prepared by other casting processes.<sup>[27,38,57,58]</sup> The

**TABLE 7** Summary of the microstructure features and their roles on the corrosion resistance of the investigated alloys

Factors	Effect	Degree of importance	
		AZ91D	MRI153M
Al content difference between fine and coarse $\alpha$ -Mg	Driving for corrosion advance	Decreases the formation of localised corrosion sites in the microstructure	Lower fraction of injected solid might originate sites of intensive localised corrosion
$\text{Al}_{12}\text{Mg}_{17}$ phase	Microgalvanic corrosion	Plays a minor role	Plays a minor role
$\text{Al}_{12}\text{Mg}_{17}$ phase	Barrier effect	Plays some role only in regions where the network of $\text{Al}_{12}\text{Mg}_{17}$ is continuous	Plays a minor or nearly no role since the network of $\text{Al}_{12}\text{Mg}_{17}$ is discontinuous
Presence of Ca	Pathway for corrosion propagation throughout the grain boundary	–	Local $\alpha$ -Mg dissolution and possibly local enhancement of corrosion rate
Presence of Ca	Formation of a more stable corrosion products layer	–	This is a beneficial effect. It is overdominated by the local partial dissolution of $\alpha$ -Mg matrix in Ca-rich areas

thixomolded MRI153M exhibited a slightly higher corrosion rate compared with AZ91D, but still low compared with similar alloys reported earlier. The combination of several factors influencing corrosion mechanisms can explain first the high corrosion resistance exhibited by the investigated thixomolded alloys and the higher corrosion resistance of the AZ91D in comparison to the MRI153M. The volume ratio of primary to secondary  $\alpha$ -Mg matrix that differs in Al content acts as one of the main driving forces for corrosion. However, since the only difference between these regions is the Al content, the driving force for corrosion is expected to be notably smaller compared with an ingot-cast material, where localised corrosion plays an important role. The higher ratio of primary/secondary  $\alpha$ -Mg matrix is attributed to eliminate or hinder other localised corrosion effects, thus enhancing the corrosion resistance of the AZ91D alloy.

The effect of the  $\beta$ -phase on the corrosion resistance seems to be marginal for the thixomolded AZ91D and MRI153M. The local dissolution of the  $\alpha$ -Mg in the vicinity of the grain boundaries of the fine secondary  $\alpha$ -Mg for the MRI153M seems to be more related to the preferential dissolution of Ca-rich region rather than the microgalvanic effect of the  $\beta$ -phase. However, the partial hindering of the corrosion front propagation in the case of the AZ91D in specific regions suggests that the  $\beta$ -phase could also have contributed to enhancing the corrosion resistance of the AZ91 in contrast to the MRI153M (Table 7).

## ACKNOWLEDGEMENTS

Helmholtz-Zentrum Geesthacht acknowledge the German Ministry of Education and Research for the provision of financial support within the framework of the proposal O2PJ2792 and Neue Materialien Fürth GmbH also acknowledge the German Ministry of Education and Research for the provision of financial support within the framework of the proposal O2PJ2791. Ricardo H. Buzolin acknowledges CD-Laboratory for Design of High-Performance Alloys by Thermomechanical Processing for the support by the Christian Doppler Society.

## ORCID

Ricardo H. Buzolin  <http://orcid.org/0000-0002-3955-6917>

## REFERENCES

- [1] D. Magers, J. Willekens *Magnesium Alloys and Their Applications* (Eds: B. L. Mordike, K. U. Kainer), Werkstoffinformationsgesellschaft mbH, Weinheim, Germany **1998**, p. 105.
- [2] R. Fink *Magnesium: Eigenschaften, Anwendungen und Potentiale* (Ed: K. U. Kainer), Wiley-VCH, Weinheim, Germany **2000**, p. 26.
- [3] S. Erickson, in Proc. of the 44th World Magnesium Conference. 1987, p. 39.
- [4] J. B. Patel, Y. Q. Liu, G. Shao, Z. Fan, *Mater. Sci. Eng., A* **2008**, 476, 341.
- [5] R. Arrabal, B. Mingo, A. Pardo, M. Mohedano, E. Matykina, I. Rodríguez, *Corros. Sci.* **2013**, 73, 342.
- [6] H. V. Atkinson, *Prog. Mater. Sci.* **2005**, 50, 341.
- [7] F. Czerwinski, *Mater. Sci. Eng., A* **2005**, 404, 19.
- [8] F. D'Errico, B. Rivolta, R. Gerosa, G. Perricone, *JOM* **2008**, 60, 70.
- [9] Regulation (EU) No 517/2014 of the European Parliament and of the Council of 16 April 2014 on fluorinated greenhouse gases and repealing Regulation (EC) No 842/2006. p. 195.
- [10] M. B. Yang, F. S. Pan, R. J. Cheng, J. Shen, *Trans. Nonferrous Met. Soc. China* **2008**, 18, 566.
- [11] A. R. A. McLelland, N. G. Henderson, H. V. Atkinson, D. H. Kirkwood, *Mater. Sci. Eng., A* **1997**, 232, 110.
- [12] R. Bigot, V. Favier, C. Rouff, *J. Mater. Process. Technol.* **2005**, 160, 43.
- [13] T. Liu, Q. Wang, A. Gao, C. Zhang, C. Wang, J. He, *Scr. Mater.* **2007**, 57, 992.
- [14] M. Qian, *Acta Mater.* **2006**, 54, 2241.
- [15] G. H. Su, Z. Y. Cao, Y. B. Liu, Y. H. Wang, L. Zhang, *Trans. Nonferrous Met. Soc. China* **2010**, 20, s402.
- [16] J. C. Gebelin, M. Suery, D. Favier, *Mater. Sci. Eng., A* **1999**, 272, 134.
- [17] C. D. Yim, K. S. Shin, *Mater. Sci. Eng., A* **2005**, 395, 226.
- [18] O. Lashkari, R. Ghomashchi, *Mater. Des.* **2007**, 28, 1321.
- [19] G. L. Makar, J. Kruger, *J. Electrochem. Soc.* **1990**, 137, 414.
- [20] C. B. Baliga, P. Tsakiroopoulos, *Mater. Sci. Technol.* **1993**, 9, 513.
- [21] A. Pardo, M. C. Merino, A. E. Coy, F. Viejo, R. Arrabal, S. Feliú Jr, *Electrochim. Acta* **2008**, 53, 7890.
- [22] S. Mathieu, C. Rapin, J. Steinmetz, P. Steinmetz, *Corros. Sci.* **2003**, 45, 2741.
- [23] G. L. Song, A. Atrens, *Adv. Eng. Mater.* **1999**, 1, 11.
- [24] C. Do Lee, C. S. Kang, K. S. Shin, *Met. Mater.* **2000**, 6, 351.
- [25] O. Lunder, J. E. Lein, T. K. Aune, K. Nisancioglu, *Corrosion* **1989**, 45, 741.
- [26] A. J. López, C. Taltavull, B. Torres, E. Otero, J. Rams, *Corrosion* **2013**, 69, 497.
- [27] G. Song, A. Atrens, X. Wu, B. Zhang, *Corros. Sci.* **1998**, 40, 1769.
- [28] G. Song, D. StJohn, *J. Light Met.* **2002**, 2, 1.
- [29] R. K. S. Raman, *Metall. Mater. Trans. A* **2004**, 35, 2525.
- [30] M. O. Pekguleryuz, A. A. Kaya, *Adv. Eng. Mater.* **2003**, 5, 866.
- [31] G. Wu, Y. Fan, H. Gao, C. Zhai, Y. P. Zhu, *Mater. Sci. Eng., A* **2005**, 408, 255.
- [32] B. Tang, X. S. Wang, S. S. Li, D. B. Zeng, R. Wu, *Mater. Sci. Technol.* **2005**, 21, 574.
- [33] N. D. Nam, M. Z. Bian, M. Forsyth, M. Seter, M. Tan, *Corros. Sci.* **2012**, 64, 263.
- [34] E. Dabah, G. Ben-Hamu, V. Lisitsyn, D. Eliezer, K. S. Shin, *J. Mater. Sci.* **2010**, 45, 3007.
- [35] S. M. Zhu, B. L. Mordike, J. F. Nie, *Mater. Sci. Eng., A* **2008**, 483–484, 583.



- [36] K. Ozturk, Y. Zhong, L. K. Liu, A. A. Luo, *JOM* **2003**, 55, 40.
- [37] R. M. Asmussen, W. J. Binns, P. Jakupi, D. Shoesmith, *J. Electrochem. Soc.* **2014**, 161, C501.
- [38] R. Ambat, N. N. Aung, W. Zhou, *Corros. Sci.* **2000**, 42, 1433.
- [39] M. Esmaily, N. Mortazavi, M. Shahabi-Navid, J. E. Svensson, M. Halvarsson, L. Nyborg, M. Wessén, A. E. Jarfors, L. G. Johansson, *J. Electrochem. Soc.* **2015**, 162, C85.
- [40] S. Jin, E. Ghali, C. Blawert, W. Dietzel, *ECS Trans.* **2007**, 3, 295.
- [41] B. Mingo, R. Arrabal, M. Mohedano, A. Pardo, E. Matykina, A. Rivas, *J. Electrochem. Soc.* **2015**, 162, C180.
- [42] D. Zander, C. Schnatterer, *Corros. Sci.* **2015**, 98, 291.
- [43] S. Mathieu, C. Rapin, J. Hazan, P. Steinmetz, *Corros. Sci.* **2002**, 44, 2737.
- [44] R. H. Buzolin, H. Dieringa, C. Blawert, H. Frank, C. L. Mendis, A. Lohmüller, K. U. Kainer, N. Hort, *Magnesium Technology 2017*, Springer International Publishing AG, San Diego **2017**, p. 381.
- [45] M. Avedesian, H. Baker, *ASM Handbook: Magnesium and Magnesium Alloys*, ASM International, Materials Park, OH **1999**.
- [46] ASTM E112-13, Standard Test Methods for Determining Average Grain Size, ASTM International, West Conshohocken, PA, 2013.
- [47] Pearson's Crystal Data, <http://www.crystalimpact.com/pcd/> (accessed: April 2019).
- [48] CaRIne Crystallography Software, <http://carine.crystallography.pagesperso-orange.fr/> (accessed: April 2019).
- [49] G. Song, A. Atrens, *Adv. Eng. Mater.* **2003**, 5, 837.
- [50] G. Song, A. Atrens, D. StJohn, *An Hydrogen Evolution Method for the Estimation of the Corrosion Rate of Magnesium Alloys*, in *Magnesium Technology 2001*, John Wiley & Sons, Inc, Hoboken, NJ **2013**, p. 254.
- [51] S. V., Lamaka, B., Vaghefnazari, Di Mei, R. P., Petrauskas, D., Höche, M. L., Zheludkevich, *Corros. Sci.* **2017**, 128, 224.
- [52] K. Ogle, S. Weber, *J. Electrochem. Soc.* **2000**, 147, 1770.
- [53] H. Eibisch, A. Lohmüller, N. Kömpel, R. F. Singer, *Int. J. Mater. Res.* **2008**, 99, 56.
- [54] F. Czerwinski, A. Zielinska-Lipiec, *Acta Mater.* **2005**, 53, 3433.
- [55] Y. F. Zhang, Y. B. Liu, Z. Y. Cao, Q. Q. Zhang, L. Zhang, *J. Mater. Process. Technol.* **2009**, 209, 1375.
- [56] W. Qudong, C. Wenzhou, Z. Xiaoqin, L. Yizhen, D. Wenjiang, Z. Yanping, X. Xiaoping, M. Mabuchi, *J. Mater. Sci.* **2001**, 36, 3035.
- [57] M. C. Zhao, M. Liu, G. Song, A. Atrens, *Corros. Sci.* **2008**, 50, 1939.
- [58] G. Song, A. Atrens, M. Dargusch, *Corros. Sci.* **1998**, 41, 249.
- [59] V. Shkirskiy, A. D. King, O. Gharbi, P. Volovitch, J. R. Scully, K. Ogle, N. Birbilis, *ChemPhysChem* **2014**, 16, 536.
- [60] A. Pardo, M. C. Merino, A. Ef Coy, R. Arrabal, F. Viejo, E. Matykina, *Corros. Sci.* **2008**, 50, 823.
- [61] F. Czerwinski, A. Zielinska-Lipiec, P. J. Pinet, J. Overbeeke, *Acta Mater.* **2001**, 49, 1225.
- [62] A. Tissier, D. Apelian, G. Regazzoni, *J. Mater. Sci.* **1990**, 25, 1184.
- [63] D. W. H. Rankin, *Crystallogr. Rev.* **2009**, 15, 223.

**How to cite this article:** Buzolin RH, Volovitch P, Maltseva A, et al. Thixomolded AZ91D and MRI153M magnesium alloys and their enhanced corrosion resistance. *Materials and Corrosion*. 2020;1–13. <https://doi.org/10.1002/maco.201911327>